

Low-cost laser speckle contrast imaging of blood flow using a webcam

Lisa M. Richards, S. M. Shams Kazmi, Janel L. Davis, Katherine E. Olin, and Andrew K. Dunn*

Department of Biomedical Engineering, The University of Texas at Austin, Austin, TX, 78712, USA

*adunn@mail.utexas.edu

Abstract: Laser speckle contrast imaging has become a widely used tool for dynamic imaging of blood flow, both in animal models and in the clinic. Typically, laser speckle contrast imaging is performed using scientific-grade instrumentation. However, due to recent advances in camera technology, these expensive components may not be necessary to produce accurate images. In this paper, we demonstrate that a consumer-grade webcam can be used to visualize changes in flow, both in a microfluidic flow phantom and *in vivo* in a mouse model. A two-camera setup was used to simultaneously image with a high performance monochrome CCD camera and the webcam for direct comparison. The webcam was also tested with inexpensive aspheric lenses and a laser pointer for a complete low-cost, compact setup (\$90, 5.6 cm length, 25 g). The CCD and webcam showed excellent agreement with the two-camera setup, and the inexpensive setup was used to image dynamic blood flow changes before and after a targeted cerebral occlusion.

©2013 Optical Society of America

OCIS codes: (120.6150) Speckle imaging; (120.3890) Medical optics instrumentation; (170.3880) Medical and biological imaging; (040.1490) Cameras.

References and links

1. A. F. Fercher and J. D. Briers, "Flow Visualization by Means of Single-Exposure Speckle Photography," *Opt. Commun.* **37**(5), 326–330 (1981).
2. A. K. Dunn, H. Bolay, M. A. Moskowitz, and D. A. Boas, "Dynamic imaging of cerebral blood flow using laser speckle," *J. Cereb. Blood Flow Metab.* **21**(3), 195–201 (2001).
3. C. Ayata, A. K. Dunn, Y. Gursoy-Ozdemir, Z. Huang, D. A. Boas, and M. A. Moskowitz, "Laser speckle flowmetry for the study of cerebrovascular physiology in normal and ischemic mouse cortex," *J. Cereb. Blood Flow Metab.* **24**(7), 744–755 (2004).
4. C. Ayata, H. K. Shin, S. Salomone, Y. Ozdemir-Gursoy, D. A. Boas, A. K. Dunn, and M. A. Moskowitz, "Pronounced hypoperfusion during spreading depression in mouse cortex," *J. Cereb. Blood Flow Metab.* **24**(10), 1172–1182 (2004).
5. H. Bolay, U. Reuter, A. K. Dunn, Z. Huang, D. A. Boas, and M. A. Moskowitz, "Intrinsic brain activity triggers trigeminal meningeal afferents in a migraine model," *Nat. Med.* **8**(2), 136–142 (2002).
6. T. Durduran, M. G. Burnett, G. Yu, C. Zhou, D. Furuya, A. G. Yodh, J. A. Detre, and J. H. Greenberg, "Spatiotemporal quantification of cerebral blood flow during functional activation in rat somatosensory cortex using laser-speckle flowmetry," *J. Cereb. Blood Flow Metab.* **24**(5), 518–525 (2004).
7. A. K. Dunn, A. Devor, A. M. Dale, and D. A. Boas, "Spatial extent of oxygen metabolism and hemodynamic changes during functional activation of the rat somatosensory cortex," *Neuroimage* **27**(2), 279–290 (2005).
8. J. D. Briers and S. Webster, "Laser speckle contrast analysis (LASCA): a non-scanning, full-field technique for monitoring capillary blood flow," *J. Biomed. Opt.* **1**(2), 174–179 (1996).
9. B. Choi, N. M. Kang, and J. S. Nelson, "Laser speckle imaging for monitoring blood flow dynamics in the *in vivo* rodent dorsal skin fold model," *Microvasc. Res.* **68**(2), 143–146 (2004).
10. J. D. Briers and A. F. Fercher, "Retinal Blood-Flow Visualization by Means of Laser Speckle Photography," *Invest. Ophthalmol. Vis. Sci.* **22**(2), 255–259 (1982).
11. A. I. Srien, Z. L. Kurth-Nelson, and E. A. Newman, "Imaging retinal blood flow with laser speckle flowmetry," *Front. Neuroenergetics* **2**, 128 (2010).
12. N. Hecht, J. Woitzik, J. P. Dreier, and P. Vajkoczy, "Intraoperative monitoring of cerebral blood flow by laser speckle contrast analysis," *Neurosurg. Focus* **27**(4), E11 (2009).
13. A. B. Parthasarathy, E. L. Weber, L. M. Richards, D. J. Fox, and A. K. Dunn, "Laser speckle contrast imaging of cerebral blood flow in humans during neurosurgery: a pilot clinical study," *J. Biomed. Opt.* **15**(6), 066030 (2010).

14. E. Klijn, H. C. Hulscher, R. K. Balvers, W. P. Holland, J. Bakker, A. J. Vincent, C. M. Dirven, and C. Ince, "Laser speckle imaging identification of increases in cortical microcirculatory blood flow induced by motor activity during awake craniotomy," *J. Neurosurg.* **118**(2), 280–286 (2013).
15. J. D. Briers, "Laser Doppler, speckle and related techniques for blood perfusion mapping and imaging," *Physiol. Meas.* **22**(4), R35–R66 (2001).
16. D. A. Boas and A. K. Dunn, "Laser speckle contrast imaging in biomedical optics," *J. Biomed. Opt.* **15**(1), 011109 (2010).
17. Y. Atchia, H. Levy, S. Dufour, and O. Levi, "Rapid multiexposure in vivo brain imaging system using vertical cavity surface emitting lasers as a light source," *Appl. Opt.* **52**(7), C64–C71 (2013).
18. B. Kruijt, H. S. Bruijn, A. van der Ploeg-van den Heuvel, H. J. Sterenborg, and D. J. Robinson, "Laser speckle imaging of dynamic changes in flow during photodynamic therapy," *Lasers Med. Sci.* **21**(4), 208–212 (2006).
19. Z. Wang, S. Hughes, S. Dayasundara, and R. S. Menon, "Theoretical and experimental optimization of laser speckle contrast imaging for high specificity to brain microcirculation," *J. Cereb. Blood Flow Metab.* **27**(2), 258–269 (2007).
20. M. M. da Silva, J. R. D. A. Nozela, M. J. Chaves, R. Alves Braga Jr, and H. J. Rabal, "Optical mouse acting as biospeckle sensor," *Opt. Commun.* **284**(7), 1798–1802 (2011).
21. M. Vannoni, M. Trivi, R. Arizaga, H. Rabal, and G. Molesini, "Dynamic speckle imaging with low-cost devices," *Eur. J. Phys.* **29**(5), 967–975 (2008).
22. I. Remer and A. Bilenca, "A cellphone-based laser speckle imager," presented at SPIE Photonics West, 8229A–15, Session 4, San Francisco, CA, 21–26 Jan. 2012.
23. L. Grimes, "Cell phone app the latest weapon in malaria detection" (2011), retrieved Mar. 4, 2013, <http://www.reuters.com/video/2011/06/08/cell-phone-app-the-latest-weapon-in-mala?videoid=212225154>.
24. O. Yang and B. Choi, "Laser speckle imaging using a consumer-grade color camera," *Opt. Lett.* **37**(19), 3957–3959 (2012).
25. G. C. Holst and T. S. Lomheim, *CMOS/CCD sensors and camera systems*, 2nd ed. (JCD Publishing and SPIE, Winter Park, FL and Bellingham, WA, 2011).
26. E. H. Ratzlaff and A. Grinvald, "A tandem-lens epifluorescence microscope: hundred-fold brightness advantage for wide-field imaging," *J. Neurosci. Methods* **36**(2-3), 127–137 (1991).
27. W. J. Tom, A. Ponticorvo, and A. K. Dunn, "Efficient processing of laser speckle contrast images," *IEEE Trans. Med. Imaging* **27**(12), 1728–1738 (2008).
28. J. R. Anderson, D. T. Chiu, R. J. Jackman, O. Cherniavskaya, J. C. McDonald, H. Wu, S. H. Whitesides, and G. M. Whitesides, "Fabrication of Topologically Complex Three-Dimensional Microfluidic Systems in PDMS by Rapid Prototyping," *Anal. Chem.* **72**(14), 3158–3164 (2000).
29. A. B. Parthasarathy, W. J. Tom, A. Gopal, X. J. Zhang, and A. K. Dunn, "Robust flow measurement with multi-exposure speckle imaging," *Opt. Express* **16**(3), 1975–1989 (2008).
30. A. Roggan, M. Friebel, K. Dorschel, A. Hahn, and G. Muller, "Optical Properties of Circulating Human Blood in the Wavelength Range 400-2500 nm," *J. Biomed. Opt.* **4**(1), 36–46 (1999).
31. B. D. Watson, W. D. Dietrich, R. Busto, M. S. Wachtel, and M. D. Ginsberg, "Induction of reproducible brain infarction by photochemically initiated thrombosis," *Ann. Neurol.* **17**(5), 497–504 (1985).
32. S. Zhang and T. H. Murphy, "Imaging the impact of cortical microcirculation on synaptic structure and sensory-evoked hemodynamic responses in vivo," *PLoS Biol.* **5**(5), e119 (2007).
33. R. Bandyopadhyay, A. S. Gittings, S. S. Suh, P. K. Dixon, and D. J. Durian, "Speckle-visibility spectroscopy: A tool to study time-varying dynamics," *Rev. Sci. Instrum.* **76**(9), 093110 (2005).
34. S. Klein, M. Staring, K. Murphy, M. A. Viergever, and J. P. Pluim, "elastix: a toolbox for intensity-based medical image registration," *IEEE Trans. Med. Imaging* **29**(1), 196–205 (2010).
35. S. M. S. Kazmi, A. B. Parthasarthy, N. E. Song, T. A. Jones, and A. K. Dunn, "Chronic imaging of cortical blood flow using Multi-Exposure Speckle Imaging," *J. Cereb. Blood Flow Metab.* **33**(6), 798–808 (2013).
36. S. J. Kirkpatrick, D. D. Duncan, and E. M. Wells-Gray, "Detrimental effects of speckle-pixel size matching in laser speckle contrast imaging," *Opt. Lett.* **33**(24), 2886–2888 (2008).
37. Logitech, "Logitech USB Video Class (UVC) Device Feature list" (2009), retrieved May 3, 2013, http://wayback.archive.org/web/20110916202227/http://www.quickcamteam.net/devices/logitech_uvc_device_feature_list_by_device.pdf.
38. L. Song and D. S. Elson, "Effect of signal intensity and camera quantization on laser speckle contrast analysis," *Biomed. Opt. Express* **4**(1), 89–104 (2013).

1. Introduction

Recently, there has been great interest in using laser speckle contrast imaging (LSCI) as a tool for imaging flow in preclinical research and clinical applications. LSCI is a full field, real-time optical imaging method with high spatial and temporal resolution that can be used to image dynamic changes in blood flow. Although first introduced in the early 1980s [1], LSCI was not widely adopted by researchers until the last decade. LSCI has been applied in cerebral blood flow studies of stroke [2, 3], cortical spreading depression [4, 5], and functional activation [6, 7] in animal models. LSCI has also been investigated for clinical use in skin [8, 9], retina [10, 11], and neurosurgical applications [12–14].

Laser speckle is the random interference pattern produced when coherent light scatters from a random medium and can be imaged onto a camera detector. When imaging a turbid medium that contains moving scatterers, such as red blood cells in cortical vessels, the speckle pattern fluctuates in time as a result of time-varying phase shifts in the backscattered light. Temporal and spatial intensity variations of the random speckle pattern contain information about the motion of the scattering particles and can be analyzed to estimate blood flow information [15, 16]. Spatial speckle contrast analysis quantifies the local spatial variance, or blurring, of the speckle pattern that results from blood flow. Areas with greater motion have more rapid intensity fluctuations and therefore have more blurring of the speckles during the camera exposure time, which can be quantified in the calculation of the speckle contrast.

LSCI utilizes very simple instrumentation to perform non-contact blood flow imaging, which makes the technique appealing to both scientific researchers and clinicians. The instrumentation simply includes a laser for illuminating the tissue surface, a camera for detection of the backscattered light, and imaging optics to focus the light onto the camera sensor. Although the instrumentation required for LSCI is very simple, there are wide variations in the component specifications used by researchers across the field. For example, the cameras used for LSCI vary from cost-effective monochrome CMOS or CCD sensors [2, 9, 13] to expensive cooled CCDs [6, 11, 17–19], with little justification provided for the camera choice. There is always interest in reducing the cost of imaging methods to improve ease of integration and increase adoption for both laboratory research and clinical applications. Other groups have begun examining the possibility of using low-cost devices (<\$100) to perform LSCI for medical applications in tracking skin movement and movement of an artificial eye [20]. In addition, the low-cost devices have also been used to explore non-medical applications such as monitoring wood deformation, paint drying, and membrane vibration [20, 21]. These studies were performed using a low-cost camera sensors and low power (5-8 mW) laser sources. One group has investigated the possibility of using a cell-phone camera to perform LSCI for assessing blood perfusion in human skin and for *in vitro* malaria detection [22]; however, the optics and illumination used were not low-cost [23]. We hypothesized that the entire LSCI system could be composed of very inexpensive instrumentation for accurate imaging of microcirculatory flows. We tested this hypothesis using low-cost components, a webcam for the camera, low-cost aspheric lenses as the imaging optics, and a laser pointer for illumination, and examined the performance relative to a traditional LSCI system.

Because we used a webcam for the camera sensor, we have to consider the differences in color vs. monochrome camera sensors. Recently, a consumer-grade color camera (digital single-lens reflex, or dSLR) was used to perform LSCI and was shown to provide similar maps of blood flow relative to a scientific-grade monochrome camera [24]. The difference in our study is the price of the color sensor (\$35 vs. ~\$2000) and the bit depth (8-bit vs. 14-bit), but the principles they describe for image analysis are the same. Briefly, the pixels of a color camera are covered with individual filters that allow mostly red (R), green (G), or blue (B) light through to the pixels, with the arrangement of the filters known as the Bayer matrix. Many webcams stream video in RGB color mode, which uses image-processing algorithms to interpolate an R, G, and B value for each pixel of the sensor (3D matrix). These interpolation algorithms vary between manufacturers, as each uses different methods to reduce color aliasing and improve color quality [25]. The webcam sensor that we chose also allowed raw streaming of Bayer data, which provides a 1D matrix containing the brightness of each individual pixel. Both modes were tested in this study, with the red color plane used for color mode and the red-filtered pixels used for Bayer mode during calculation of the speckle contrast values. Because of the arrangement of the Bayer matrix of filters on the webcam sensor, Bayer mode effectively reduces the number of pixels by 75%, but this mode provides pixel intensity values that closely match the measurement provided by traditional monochrome cameras.

In this paper, we evaluate the webcam as a potential camera sensor for imaging flow in an *in vitro* phantom as well as *in vivo* in a mouse cerebral cortex by directly comparing images recorded simultaneously from a high performance monochrome CCD camera. We also assess the feasibility of a complete inexpensive LSCI system using the webcam in combination with low-cost lenses and a laser pointer for illumination, again both *in vitro* and *in vivo*.

2. Methods

2.1 Instrumentation

To validate that low-cost camera sensors can be used for LSCI, a two-camera setup was used to allow simultaneous imaging with a monochrome CCD camera (Basler Pilot piA640-210gm, \$2000) and a color webcam (Logitech Webcam C500, \$35). A schematic of the two-camera setup is shown in Fig. 1(A). The webcam sensor was disassembled from its housing and the wide-field lens was removed and replaced with a S-mount lens holder (M12 Lenses, PT-LH010M). For the two-camera setup, a S-mount to C-mount adapter (Edmund Optics, 63-974) was used to connect with the imaging optics. Three Nikon AF-Nikkor 50 mm lenses were used for the imaging optics to obtain 1:1 imaging with both cameras, and the Nikon F-mount was adapted to C-mount to connect with both cameras. The Nikon lenses were placed in tandem, and set to infinity focus. This setup was first reported by Ratzlaff et al. [26] and was used because it provided high light collection efficiency and because it allowed individual control of the $f/\#$ for each camera arm. A 50-50 beamsplitter (Thorlabs BSW30) was placed between the first and second lenses in each imaging arm. A 660 nm laser diode (Thorlabs ML101J27) was mounted in a temperature-controlled housing (Thorlabs LDM21) and expanded using an aspheric lens to evenly illuminate the sample. For the animal experiment, a 532 nm laser (AixiZ, 200 mW) was used in combination with Rose Bengal to induce a localized occlusion in a photo-thrombotic stroke model. The green laser was attenuated using neutral density filters so that ~ 14 mW reached the tissue surface, and a long focal length plano-convex lens was used to focus the beam to a small spot in the imaging field of view. To reduce the green light that reached the camera sensors, a red filter (Edmund Optics, R-60 Long pass filter, 2") was placed before the first lens.

The schematic of the low-cost, compact setup is shown in Fig. 1(B). The webcam is imaged using two replicated aspheric lenses with 10 mm diameter and 40 mm effective focal lengths (Edmund Optics, 68-118, \$25 each) to achieve 1:1 imaging. The lenses were mounted directly to the S-mount lens holder using S-mount components from Edmund Optics for simplicity. In the future, these mounting components could be customized to reduce cost, and thus the costs of the mounting components are not included in the calculation of overall system cost. A 650 nm laser pointer (AixiZ, 5 mW, \$5) was used for illumination, and the beam was expanded using an aspheric lens to evenly illuminate the sample. The cost of all of the major components in setup 1B equals \$90, which is almost 40 times less than the cost of traditional LSCI components used in setup 1A (\sim \$3500 for the CCD camera, Nikon lenses, laser diode driver, mount, and laser diode). The length from the top of the webcam board to bottom of the lens system was 5.6 cm and the weight of the imaging setup was 25 g, which makes the system not only low-cost but also compact and light. Similar to the setup in Fig. 1(A), a green laser was directed toward the sample for the animal experiment, and a red filter (0.5") was used to reduce the green light that reached the camera sensor.

To achieve a fair comparison between setups 1A and 1B, the speckle size was matched between the two setups and between the two cameras. The $f/\#$ of setup 1B could not be easily adjusted and was used to limit the $f/\#$ for the webcam arm of setup 1A. The $f/\#$ of setup 1B was calculated to be 4.44 (focal length = 40 mm, limiting aperture diameter = 9 mm). Thus, the Nikon lens on the webcam arm was set to an $f/\#$ of 4 for the two-camera experiment. The pixel size for the webcam CMOS sensor was calculated to be 2.8 μm . Based on preliminary measurements of the speckle size using the 1:1 tandem lens configuration, the speckle size was most closely related to the expression $1.22\lambda f/\#M$. Thus, the speckle size was approximately 1.15 pixels for the webcam setup using an $f/\#$ of 4. The CCD camera had a

pixel size of $7.4\ \mu\text{m}$, thus the $f/\#$ for the CCD arm was set to 11 to get a speckle size of approximately 1.20 pixels.

Each camera was controlled using a separate computer using custom software. The CCD camera was controlled using the Basler Pylon API (Basler Inc.), while the webcam was controlled using the NI IMAQdx library (National Instruments Inc.). By integrating the source code from freely available software from Logitech (bayer.exe) into our custom software, the webcam could be easily switched between color and Bayer modes. By incorporating rapid processing techniques into the custom software [27], the speckle contrast images were computed and displayed in real-time during the procedure for both cameras. The custom software was modified to allow correct computation of the speckle contrast values for the webcam in both color and Bayer modes for real-time display.

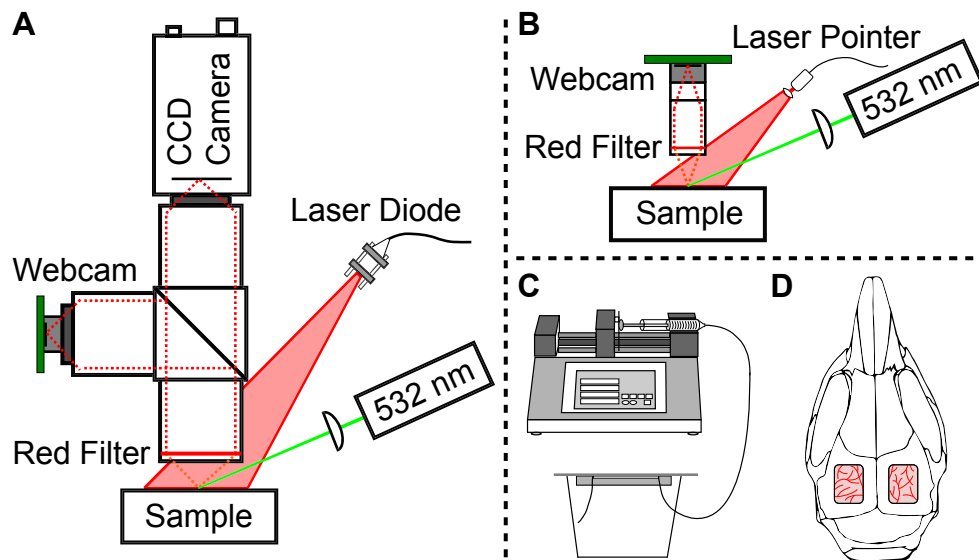


Fig. 1. (A) Schematic of the two-camera setup for simultaneous laser speckle imaging with a CCD camera and a webcam using traditional optics and illumination components. A 50-50 beamsplitter separates the light between the two imaging arms. (B) Schematic of the low-cost, compact laser speckle imaging system, where the lenses are inexpensive aspheres and the illumination is a laser pointer. In both (A) and (B), the 532 nm laser is only used for the animal study. (C) and (D) illustrate the two different samples assessed in this study. (C) A microfluidic flow phantom is used for *in vitro* validation and different flow levels are controlled using a syringe pump. (D) *In vivo* validation is performed using a mouse prepared with bi-lateral cranial windows for assessment of setup (A) and (B), respectively.

2.2 Microfluidic study procedure

The instrumentation in setups 1A and 1B were used to sequentially image a microfluidic flow phantom for *in vitro* validation, as shown in Fig. 1(C). The microfluidic flow phantom comprised of a $200\ \mu\text{m}$ square channel embedded in poly dimethyl siloxane (PDMS) with titanium dioxide (TiO_2) added to generate a scattering background that mimicked tissue optical properties. The channel was fabricated using the rapid prototyping technique [28] and was bonded to a glass slide to seal the channel, similar to the procedure described in [29]. The microfluidic phantom was connected to a syringe pump (Cole-Parmer, 74905-04) using silicone tubes. A 1 mL syringe holding a $\mu\text{s} = 243\ \text{cm}^{-1}$ suspension of $1\ \mu\text{m}$ diameter polystyrene beads (Thermo Scientific, 5100A) was pumped through the microfluidic channel at controlled rates using the syringe pump. The scattering concentration of the beads was chosen to mimic the scattering properties of whole blood. Since the polystyrene beads have a lower anisotropy than blood ($g = 0.9176$ vs. $g = 0.98$), the reduced scattering coefficient was matched to that of flowing blood assuming a hematocrit level of 50% and an oxygen

saturation >98% [30]. The corresponding scattering coefficient of the beads was derived using the anisotropy of the polystyrene beads and the matched reduced scattering coefficient. Prior to placement in the syringe, sonication was used to fully suspend the particles in the solution and to remove any bubbles that may disrupt consistent flow rates. Flow rates from 1–10 mm/s were examined in 1 mm/s increments. The same solution and syringe pump settings were used for both setups 1A and 1B for comparison.

Images were recorded for 3 minutes, starting 30 seconds after starting each flow rate, and the average and standard deviation over this time period were used for assessment. Images were recorded sequentially using both color mode and Bayer mode for comparison. For the two-camera setup in 1A, a neutral density filter was placed in front of one of the cameras to match the raw image histogram peaks (histogram range = 255). The neutral density filter was placed in front of the webcam during color mode (optical density = 0.6, webcam peak = 125, CCD peak = 120) and in front of the CCD during Bayer mode (optical density = 0.3, webcam peak = 45, CCD peak = 50). For the setup in 1B, the illumination was adjusted to match the webcam raw image histograms from setup 1A (color mode peak = 135, Bayer mode peak = 40). In all cases, histogram peaks differed by <10 intensity counts between the two cameras and setups during the *in vitro* imaging sessions.

2.3 Animal study procedure

The instrumentation in setups 1A and 1B were also used to sequentially image bilateral cranial windows in a single mouse for *in vivo* validation, as shown in Fig. 1(D).

The mouse (CD-1, male, 25-30g, Charles River) was anesthetized with 80% N₂/O₂ vaporized isoflurane (2-3%) via nosecone. Temperature was maintained at 37°C with a feedback heating plate (World Precision Instruments Inc., Sarasota, FL). Prior to bilateral craniectomy, the mouse was administered carprofen (5mg/kg, subcutaneous) and dexamethasone (2mg/kg, intramuscular) for anti-inflammation and restriction of edema after skull removal, respectively. The mouse was placed supine and the head fixed to a stereotaxic frame (Narishige Scientific Instrument Lab, Tokyo, Japan). The scalp was shaved and resected to expose skull between bregma and lambda skull sutures. A 3-4 mm diameter portion of skull was removed from each hemisphere with a dental drill (Ideal Microdrill, 0.8mm burr, Fine Science Tools, Foster City, CA) with frequent ACSF perfusion. Cyanoacrylate (Vetbond, 3M, St. Paul, MN) was added to exposed skull areas to facilitate dental cement adhesion. A 5-8mm round cover glass (#1.5) with a layer of ACSF was placed over the exposed brain on each hemisphere. A dental cement mixture was wicked around the perimeter of the cover glass and sealed to surrounding skull. The animal was allowed to recover from anesthesia and was monitored for cranial window integrity and behavior normality. For imaging, the mouse was anesthetized with 1.5-2% vaporized isoflurane in N₂/O₂ (80/20) and remained under nosecone inhalation while in the stereotaxic frame.

For *in vivo* imaging, only Bayer mode was used based on the results from the *in vitro* testing. A neutral density filter was placed in front of the CCD for histogram matching in setup 1A (optical density = 0.3). For both setups 1A and 1B, the illumination was adjusted so that the raw histogram peaks differed by <11 intensity counts during both *in vivo* imaging sessions (CCD peak = 68, webcam setup 1A peak = 57, webcam setup 1B = 46). Each imaging setup was examined sequentially, using the right cranial window for the two-camera comparison in 1A and the left cranial window for the inexpensive setup in 1B. The anesthetized mouse was placed under each imaging setup and the desired cranial window was aligned in the camera field of view. Baseline images were recorded for at least 5 minutes, then the mouse was administered Rose Bengal (0.15 mL, 15 mg/mL, intraperitoneal), which is a photothrombotic agent that produces vascular clots [31, 32]. After 2 minutes, green laser light illuminated the tissue surface to activate the Rose Bengal and initiate the clotting cascade. Although a red filter was used to block the green light from the cameras, the laser intensity was high enough to bleed through the filter and accurate LSCI images could not be obtained during green laser irradiation. Therefore, the green laser was modulated using a

function generator so that it was on for 15 seconds and off for 5 seconds in a repeating cycle to allow imaging throughout the formation of the occlusion.

For the first imaging session using setup 1A, the green laser was modulated for 19 minutes and then the function generator was turned off so that the laser was constantly illuminating the tissue. A second bolus of Rose Bengal (0.15 mL, 15 mg/mL, intraperitoneal) was administered 3 minutes after the modulation was turned off to help solidify clot formation. After the clot appeared stable in LSCI, the green laser was turned off and post-occlusion images were recorded for 15 minutes. For the second imaging session using setup 1B, the webcam was transferred to the inexpensive optics and the laser pointer was adjusted to illuminate the left cranial window. Approximately 1 hour elapsed between the first and second imaging sessions during the change in setup. A third bolus of Rose Bengal (0.15 mL, 15 mg/mL, intraperitoneal) was administered after baseline images were acquired and the green laser modulation commenced 2 minutes after the injection. For this setup, the green laser was less focused and spread out over a larger area on the tissue surface, which made clot formation difficult while modulating the laser. Thus, the green laser modulation was stopped after only 5 minutes and the laser was allowed to constantly illuminate the tissue for 33 minutes to form the occlusion. Similar to setup 1A, the green laser was turned off after the clot appeared stable and post-occlusion images were recorded for 15 minutes.

2.4 Image analysis

The raw images recorded by the camera were converted to speckle contrast images using Eq. (1), where the speckle contrast K is defined as the ratio of the standard deviation, σ_s , and the mean intensity of pixels, $\langle I \rangle$, in a small region of the image,

$$K = \frac{\sigma_s}{\langle I \rangle} \quad (1)$$

The speckle contrast image was calculated by computing this ratio in a 7x7 pixel region centered at every pixel and sliding this window across the raw image. Speckle contrast images were computed, saved, and displayed in real-time during acquisition [27].

The rest of the image analysis was performed in post-processing after the completion of the experiments. Speckle contrast images were converted to correlation time, τ_c , which is considered a more quantitative measure of blood flow [8]. The correlation time is the average decay time of the light intensity autocorrelation function. Faster speeds cause the autocorrelation time to decrease faster, giving a smaller value for τ_c [15]. Thus, the correlation time is inversely related to the speed of the moving scatterers, which are red blood cells for the case of blood flow imaging [8]. The measured speckle contrast value K is fitted for its corresponding correlation time value, τ_c , at each pixel using Eq. (2),

$$K(T, \tau_c) = \left(\beta \frac{e^{-2x} - 1 + 2x}{2x^2} \right)^{1/2}, \quad (2)$$

where $x = T/\tau_c$, T is the exposure time of the camera (5.0 ms in this study), τ_c is the correlation time, and β is an instrumentation factor that accounts for speckle sampling, polarization, and coherence effects [33]. For the purposes of these experiments, β was assumed to be equal to 1, and relative changes in flow were computed using an average of the initial frames as the baseline ($\text{flow} = \tau_{c, \text{baseline}} / \tau_{c, \text{current}}$) [2, 3].

For the microfluidic experiments, regions of interest (ROIs) were chosen within the channel such that the ROIs covered the same physical area for each camera sensor. For the two-camera *in vivo* experiment, images obtained from each camera were anatomically co-registered using an affine transform so that the images from both techniques could be easily compared. Because tissue deformation occurred following the ischemic event in both *in vivo* experiments, the images acquired after the stroke were registered to the baseline images using a B-spline transform applied using *Elastix*, an open source software package for medical

image registration based on the Insight Segmentation and Registration Toolkit (ITK) [34]. This non-rigid registration allowed accurate tracking of the same tissue ROIs before and after the stroke occurred to allow visualization of the blood flow changes over time.

3. Results

3.1 Microfluidic study

Representative speckle contrast images from the microfluidic study are shown in Fig. 2, where images are shown for both the two-camera setup (1A) and the inexpensive setup (1B). The dark areas are regions of high flow, and correspond to the location of the microfluidic channel within the phantom. The ROIs used for subsequent analysis are shown in red for the color mode images and in blue for the Bayer mode and CCD images. In both setups, the webcam images acquired in color mode have a different visual appearance to those acquired in Bayer mode, which appear more similar to the images acquired from the CCD camera. Both color mode images and Bayer mode images are shown with the same color bar, respectively, for visual comparison. Image profiles are shown to allow quantitative comparison between both cameras and setups.

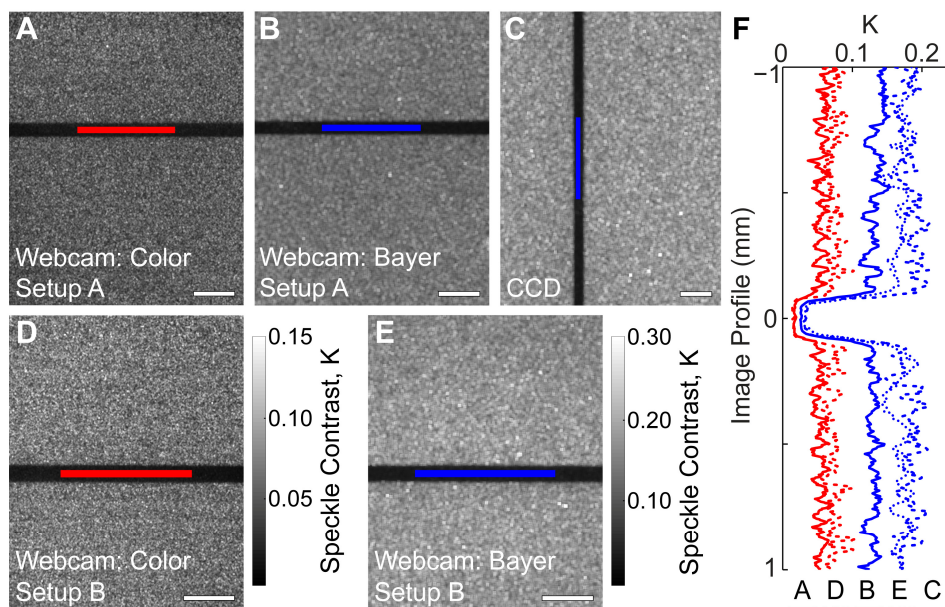


Fig. 2. Representative speckle contrast images averaged over 10 frames illustrating the location of the ROIs used for analysis (shown in red for color mode and in blue for Bayer mode and CCD images). Speckle contrast images are shown for (A) the webcam acquired in color mode within the two-camera setup (mean $K = 0.0536$), (B) the webcam acquired in Bayer mode within the two-camera setup (mean $K = 0.132$), (C) the CCD camera acquired simultaneously with the webcam in Bayer mode (mean $K = 0.167$), (D) the webcam acquired in color mode in the inexpensive setup (mean $K = 0.0676$), and (E) the webcam acquired in Bayer mode in the inexpensive setup (mean $K = 0.167$). The color bar for (D) is the same as that for (A), and the color bar for (E) is the same as that for (B) and (C). Scale bars = 0.5 mm. (F) Cropped profiles are shown for images (A-E). Each profile is averaged over 20 pixels, and is plotted in physical space (mm) with the channel locations lined up for clarity.

The two cameras have different sensor sizes (4.8 x 3.6 mm for the CCD, 3.6 x 2.9 mm for the webcam) and pixel densities (648 x 488 pixels for the CCD, 1280 x 1024 pixels for the webcam). Since we are imaging 1:1, the image field of view is approximately the same as the sensor size. The pixel resolution of the images in Fig. 2 varies from 1274 x 1018 for Figs. 2(A) and 2(D), 634 x 506 for Figs. 2(B) and 2(E), and 642 x 482 for Fig. 2(C). The resolution is smaller than the sensor resolution because the edges of the speckle contrast images are

cropped to remove edge artifacts that occur during speckle contrast calculation. The Bayer mode images are smaller than the color mode images because the red-filtered pixels have been extracted. Because all images in Fig. 2 are displayed at the same height, the color mode speckle contrast images appear to have been computed using smaller $N \times N$ regions; however, 7×7 regions were used for all images. To account for these differences in resolution and field of view, the ROIs were chosen so that they covered the same physical area ($\sim 0.09 \text{ mm}^2$) to ensure an equivalent sampling of photons in both cameras. This means that the number of pixels averaged for the ROIs in the CCD camera was fewer than that for ROIs in the webcam.

Images were acquired over 3 minutes during each speed (1–10 mm/s in 1 mm/s increments), which was ~ 18000 images for the CCD and ~ 400 images for the webcam due to differences in the frame rates. The CCD camera had a maximum frame rate of 200 fps and the webcam was operated at 5 fps at the native sensor resolution to allow proper use of the Bayer raw streaming feature. The average speckle contrast value was calculated within the ROI for each frame and this was then averaged over all frames and converted to correlation time. Thus, a single average correlation time was saved for each speed. Relative flow rates were calculated by assigning one of the speeds to be the baseline correlation time. The baseline speed was set to 2 mm/s for the two-camera setup and 3 mm/s for the inexpensive setup.

Relative flows for the CCD camera were plotted against relative flows for the webcam for the two-camera experiment in Fig. 3(A). The two axes are plotted on the same scale so that the diagonal line indicates one-to-one correspondence between the two cameras. The red dots show the results from the webcam in color mode, while the blue dots show the results from the webcam in Bayer mode. The scatter plot indicates a very close linear relationship between relative flows obtained from the CCD and the webcam in Bayer mode, whereas the webcam color mode relative flows deviate from the CCD results. Because these plots show the relative flow calculation, the axes do not match up with the speeds tested, but rather show how LSCI measures the differences in speeds. Thus, relative to 2 mm/s, the relative flow ranges from 0.67 – 1.57 in the Bayer mode plot and from 0.82 – 1.40 in the color mode plot.

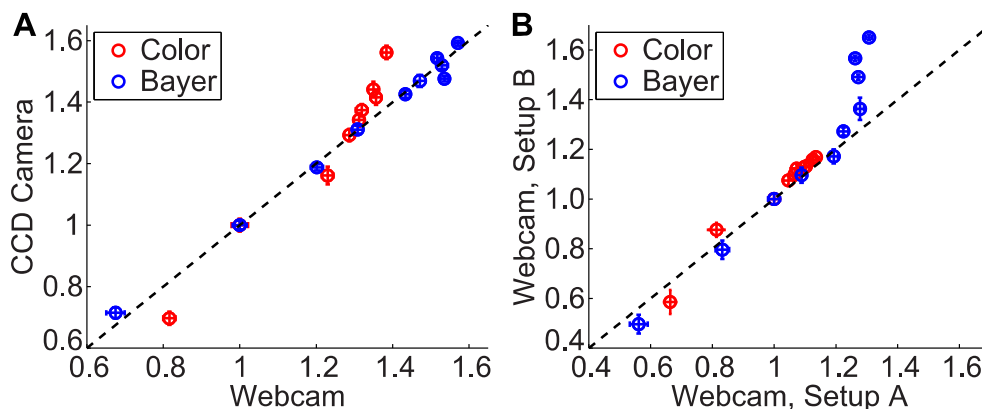


Fig. 3. Scatter plots illustrating the relative flow changes between different speeds of the microfluidic experiment, with a direct comparison between the CCD camera and the webcam in (A), and the webcam in the inexpensive setup vs. the two-camera setup in (B). Speed 2 was used for the baseline flow in (A), and speed 3 was used for the baseline flow in (B). Each point is the average relative flow with error bars in each direction depicting the standard deviations for each camera or setup.

Relative flows for the webcam in the two-camera setup (1A) were plotted against relative flows for the webcam in the inexpensive setup (1B) in Fig. 3(B). Because a different speed was used as the baseline value for this plot, the axes do not match up with the plot in Fig. 3(A); however, the same correlation time data was used for both plots. Relative to 3 mm/s, the relative flow ranges from 0.56 – 1.31 in the Bayer mode plot and from 0.66 – 1.14 in the color mode plot. This scatter plot indicates that the inexpensive optics do not affect the relative flows measured, at least for slower speeds 1–7 mm/s. The Bayer mode results for the

inexpensive setup deviate from those acquired from the two-camera setup for the higher speeds, but the trend indicates superior performance with the inexpensive setup. We observe that the relative flows continue to increase for higher speeds with the inexpensive setup while the relative flows from the two-camera setup level off for speeds 7–10 mm/s. This indicates that the inexpensive system had improved sensitivity to the higher flow rates relative to the two-camera setup. Although poor sensitivity was observed with the two-camera system at the higher flow rates, it was observed equally with both the CCD camera and the webcam in Bayer mode, as indicated by the excellent correspondence in Fig. 3(A), and this may be improved by using a shorter exposure time. The color mode results in Fig. 3(B) show excellent agreement between the two setups for all speeds; however, there is very little differentiation in relative flows across the different speeds. This indicates that color mode is less sensitive to changes in flow rates. Based on these results, the webcam was operated in Bayer mode for the *in vivo* experiments.

3.2 Animal study

Baseline speckle contrast images averaged over 10 frames are shown for the CCD and webcam in Figs. 4(A) and 4(B), respectively. The CCD images have been registered to match the orientation of the webcam images and both images were cropped to remove regions that are not present in both cameras. Both images are shown with the same color bar for comparison and the ROIs that are used for subsequent analysis are shown on both images. These two images demonstrate the similarity between the CCD and the webcam blood flow maps *in vivo*. The time courses of the relative flow for every ROI are shown in the plots in Figs. 4(C) and 4(D), where the average of correlation times from the first 5 minutes of acquisition was used as the baseline flow. The time course for the CCD was smoothed using a moving average filter with a window size that approximated the time it took to acquire each webcam image so that the two cameras could be compared with the same temporal resolution. The time courses from the 6 regions were split into two different plots containing the vessel regions in Fig. 4(C) and the parenchyma regions in Fig. 4(D) for clarity. Each plot has 6 lines, where the solid lines represent the time course of the relative flow calculated from the CCD and the dotted lines represent the time course of the relative flow calculated from the webcam. These plots clearly demonstrate the similarity in performance of the two cameras, as the solid and dotted lines are overlapping or very slightly offset throughout the time course.

For this experiment, we can clearly see dynamic flow changes in both cameras during minutes 9 to 27 in the time course while the green light was modulated. Initially, relative flow increases after the laser is turned on, but then the clot starts to form in the vessel with the blue ROI and reduces flow significantly. The green light was left on from 27 to 40 minutes where there is a break in the time course to solidify the vessel occlusion. Although ischemia was focused on the vessel with the blue ROI, all regions analyzed experienced a high reduction in flow after the stroke with flow rates <50% of baseline values in all cases.

To allow better visualization of the spatial extent of the occlusion, relative blood flow overlay images were generated that showed regions where relative flow was less than 35% of the baseline value overlaid on the baseline speckle contrast images. This is shown in Fig. 5(A) for the CCD and Fig. 5(B) for the webcam and illustrates that the spatial extent of the stroke was very similar as measured by both cameras. The CCD overlay shows slightly more regions colored red in the parenchyma, which indicates that the CCD measured a slightly higher reduction in flow than the webcam. The difference in the maximum reduction of flow from baseline between the two overlay images is 3%. This can be seen as a slight difference in the central vein of the overlay images and at the endpoint of the blue ROI plots in Fig. 4(C). However, these overlay images are still exceedingly similar and indicate comparable performance of the webcam relative to the CCD during an *in vivo* change in blood flow.

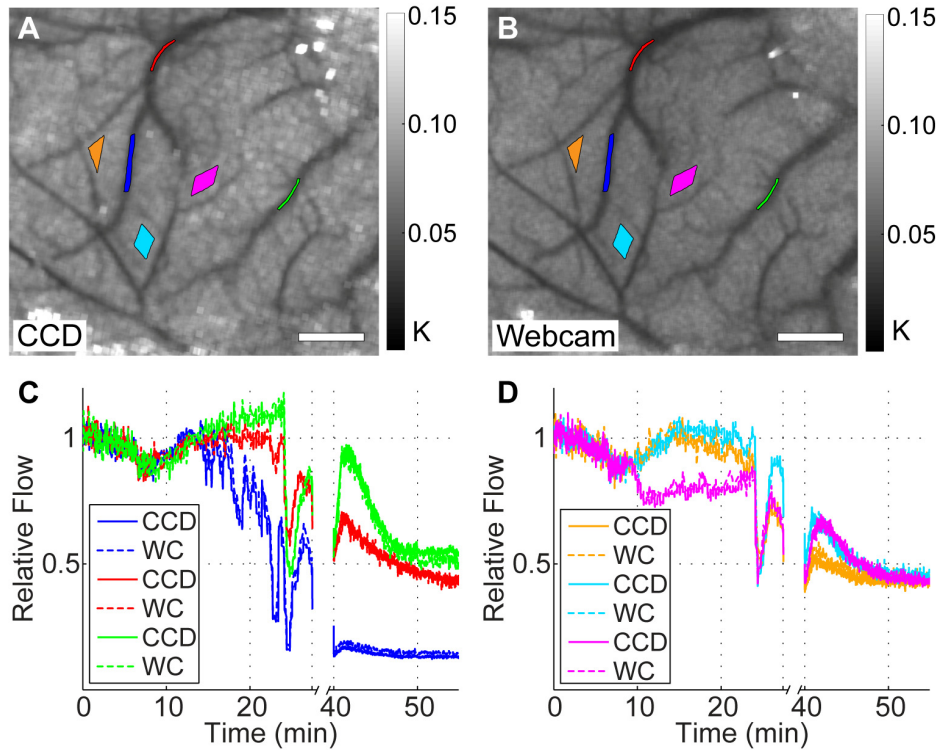


Fig. 4. Results from the two-camera *in vivo* experiment, showing registered baseline speckle contrast images for the CCD camera (A) and the webcam (B) with ROI locations used for analysis. Color bars indicate the range of speckle contrast values (K) displayed in the images. Scale bars = 0.5 mm. The plots in (C) and (D) show the time courses for the vessel and parenchyma ROIs, respectively, and show the CCD and webcam (WC) relative flows for each ROI on the same plot for direct comparison. The colors of the ROIs in (A) and (B) match the colors used for the plots in (C) and (D), and the break in the time course was when the green laser was left on continuously for clot formation.

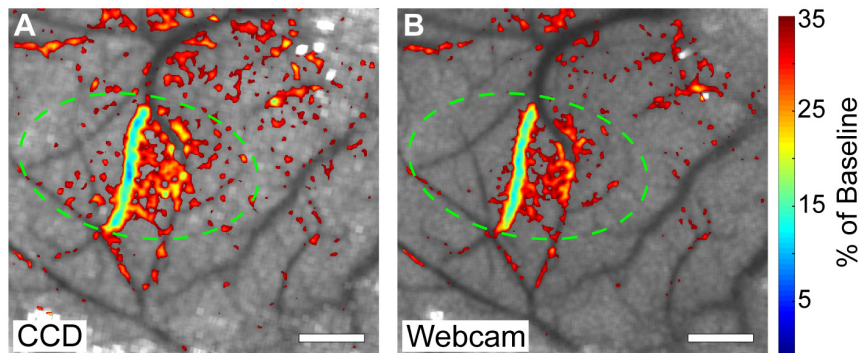


Fig. 5. Relative blood flow overlay from the two-camera *in vivo* experiment depicting the reduction in flow after the stroke overlaid over baseline speckle contrast images with a 35% reduction of baseline cutoff for the CCD camera (A) and the webcam (B). Targeted area for photothrombosis is marked with a green circle in each image. Scale bars = 0.5 mm.

Similar results were seen when the webcam was used with the complete inexpensive setup to measure a change in blood flow *in vivo*. Baseline speckle contrast images averaged over 10 frames are shown for the webcam in Fig. 6(A), along with the location of the ROIs used for

subsequent analysis. Qualitatively, the speckle contrast image from the inexpensive setup has similar quality to the webcam image obtained from the two-camera setup, despite the order of magnitude disparity in the component costs. Figure 6(B) shows the relative blood flow overlay illustrating the spatial extent of the stroke where relative blood flow was less than 35% of baseline overlaid on the baseline speckle contrast image. This figure clearly shows that the spatial extent of the stroke was much larger than in the two-camera experiment, and this occurred because the green laser spot size was more spread out in this setup.

The time courses from the 6 regions were split into two different plots in Figs. 6(C) and 6(D) for clarity. We can see a similar shape for the time course before the occlusion, where the relative flow starts to increase when the green laser is turned on at 11 minutes. The green laser was left on continuously from 17 to 50 minutes where there is a break in the time course to allow stable clot formation. The time course indicated that all regions experienced a high reduction in flow after the stroke with flow rates <50% of baseline values in all cases. As confirmed by the overlay image, the red, orange, and green vessels experienced the largest reduction in flow. The results from this experiment indicate that a \$90 setup can be used to image dynamic changes in microcirculatory blood flow during an ischemic event.

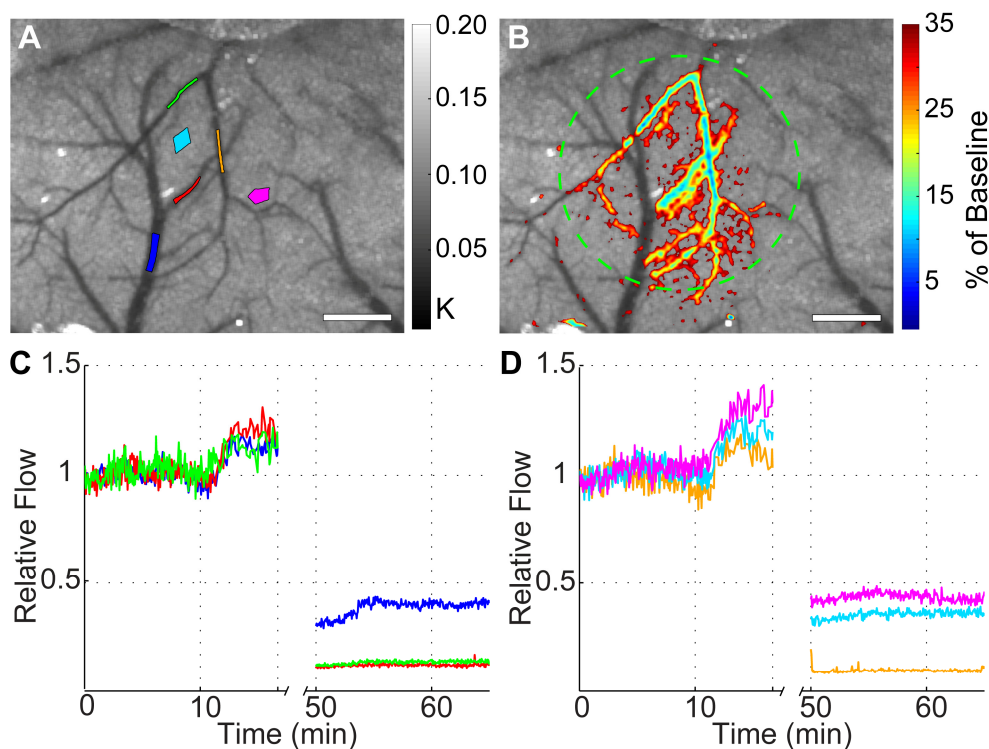


Fig. 6. Results from the inexpensive *in vivo* experiment, showing baseline speckle contrast images from the webcam with ROI locations used for analysis (A). Color bar indicates the range of speckle contrast values (K) displayed in the image. (B) Relative blood flow overlay depicting the reduction in flow after the stroke overlaid over baseline speckle contrast images with a 35% reduction of baseline cutoff. Targeted area for photothrombosis is marked with a green circle. Scale bars = 0.5 mm. The plots in (C) and (D) show the relative flow time courses for the ROIs split onto two plots for visualization. The colors of the ROIs in (A) match the colors used for the plots in (C) and (D), and the break in the time course was when the green laser was left on continuously for clot formation.

To further illustrate the utility of the webcam, we recorded images of the right cranial window within the two-camera setup 1-week after inducing the stroke. White light reflectance images were recorded with the webcam in color mode to image the vascular anatomy and a

representative image is shown in Fig. 7(A). The circled region centered over the location of the occlusion exhibited higher reflectance due to decreased absorption from blood in that region. Speckle contrast images were also recorded in Bayer mode as shown in Fig. 7(B) and excellent agreement between the vascular anatomy and the blood flow map is observed. We also see higher speckle contrast values correlating with reduced flow in the same circled region as the color image relative to the surrounding tissue. Both images indicate that vascular remodeling has taken place in the recovery period, as different vessel shapes are observed in the main vessels affected by the initial occlusion. Although we cannot draw accurate quantitative conclusions between two chronic measurements recorded with a single exposure time [35], these images indicate that the webcam has the feasibility to be used as a tool for imaging both vascular anatomy and blood flow in acute and chronic settings.

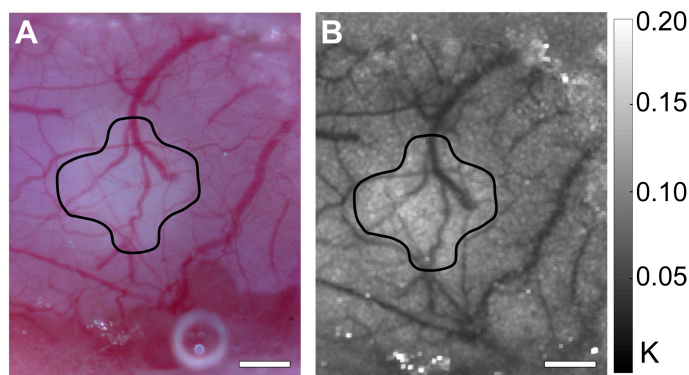


Fig. 7. The webcam was used for chronic image acquisition from the right cranial window 1-week after the stroke. (A) Color mode white light reflectance image depicting vascular anatomy and (B) speckle contrast image averaged over 10 frames showing blood flow. The drawn-in region depicts the area with reduced blood flow 1-week post stroke. Color bar indicates the range of speckle contrast values (K) displayed in the image. Scale bars = 0.5 mm.

4. Discussion

Very few studies have investigated the possibility of using low-cost devices for performing LSCI [20–22], and many groups report using relatively expensive cooled CCD cameras to perform LSCI [6, 11, 17–19]. The results of this study demonstrate that expensive instrumentation is not necessary for obtaining accurate values of relative blood flow in a microcirculatory setting, both *in vitro* and *in vivo*. For this study, the values are considered accurate relative to the traditional LSCI system examined for direct comparison composed of the high performance CCD camera, Nikon lens pair, and laser diode illumination. The relative blood flow values calculated by the webcam had significant agreement with those measured with the CCD camera, as confirmed by linear regression analysis in Table 1. We compared the linear relationship between the relative flows measured from the two cameras by calculating the R^2 value for a linear fit with a slope of 1 and intercept of 0 (perfect correspondence). These results indicate excellent correspondence between the two cameras, with an R^2 value of 0.991 *in vitro* with Bayer mode (speeds 1–10 mm/s) and R^2 values ranging from 0.958 – 0.994 for the different ROIs analyzed *in vivo*. We also compared the relative flows between the two cameras statistically using Student’s two-sample t-test. High p-values were calculated for all cases listed in Table 1 ($p > 0.3$), indicating that the two cameras are not statistically significantly different.

One observation from this study was the slight difference in the speckle contrast images acquired from the webcam versus the CCD, especially *in vivo*. This is seen when comparing Figs. 4(A) and 4(B), where the parenchyma tissue regions of the CCD image appear slightly brighter (higher speckle contrast) than those in the webcam image. This may be due to the fact that we are using every other pixel to calculate the speckle contrast image with the

webcam. Thus, the 7x7 window actually covers a larger physical area in the webcam than it does in the CCD. This also results in a reduction in the standard deviation of pixel intensities across the entire image, or effectively a narrower histogram. Thus, with the histogram peaks approximately matched, the image averages were the same, but the image standard deviations were lower for the webcam, which could explain the slightly lower speckle contrast values. Other factors that may have contributed to the differences in the speckle contrast images are the differences between the camera sensors. Because the webcam is a consumer-grade camera, the spectral sensitivity curve for the sensor is not readily available and we do not know exactly how much it differs from the CCD. The CCD camera has a detection threshold of 0 intensity counts while the webcam in Bayer mode has a detection threshold of 15 counts. Since there is a distinct difference in the detection threshold of the two sensors, the image averages were matched so that the spread of the raw histogram was above the detection threshold. Thus, the reduced standard deviation of the webcam raw images is a more reasonable explanation for the reduced speckle contrast values. One possible improvement of webcam-based LSCI is to increase the speckle size by increasing the $f/\#$. Since we are using every other pixel to calculate the speckle contrast in Bayer mode, we would get a more accurate sampling of the speckle pattern if we set the $f/\#$ such that the speckle size is at least twice the size of a pixel for speckle-pixel size matching, or at least four times the size of a pixel to satisfy the Nyquist criterion [36].

Table 1. Linear regression analysis between the measured relative flows from the webcam and CCD^a

<i>In vitro</i> Results		<i>In vivo</i> Results (Setup 1A)	
<i>Setup, Mode</i>	R^2	<i>ROI</i>	R^2
1A, Bayer ^b	0.991	Blue	0.994
1A, Color ^b	0.767	Red	0.984
1B, Bayer ^b	0.765	Green	0.958
1B, Bayer (1–7) ^c	0.971	Orange	0.983
1B, Color ^b	0.937	Cyan	0.984
		Magenta	0.984

^a R^2 values are calculated from a linear fit with slope = 1 and intercept = 0

^bCalculated using results from speeds 1–10 mm/s

^cCalculated using results from speeds 1–7 mm/s only

There are some limitations involved with using a webcam as the camera sensor for LSCI imaging. The major restriction is the maximum frame rate possible, especially when using Bayer mode. For the Logitech webcams, Bayer mode is only accurate when used at certain resolutions. For the camera model used in this study, Bayer mode could only be used at the camera sensor's native resolution (1280 x 1024, 5 fps). Many webcams use a smaller region such as VGA resolution to perform video rate imaging at 30 fps, but we cannot take advantage of this faster speed when using Bayer mode. Another limitation is that not all webcam models support Bayer mode. As of 2009, Logitech offered ~10 webcam models that support Bayer mode streaming [37], but other vendors that make USB video class (UVC) devices may also be compatible. Bayer mode support should be verified before purchase with any color camera used for LSCI. Because the bit depth of the webcam is limited to 8-bits, another limitation is that the sensitivity to small changes in flow may be reduced [38].

Another observation from this study was the comparable performance of the low-cost LSCI imaging optics and illumination components relative to their expensive counterparts. The aspheric lenses and low-power laser pointer provided images with similar quality to those obtained using the Nikon lenses and a single-mode laser diode. This implies that the differences in the imaging optics and illumination were not critical to the final results. This is

a reasonable observation assuming that the image aberrations are minimal and the coherence length of the source is sufficient in each case. In our system, chromatic aberrations are not an issue since we are using single-wavelength illumination. Spherical aberrations are also minimized due to the large $f/\#$ settings primarily chosen to control the speckle size. Thus, any image aberrations present were minimal enough so that the entire field of view was in good focus with both lens setups. The coherence length of both laser sources was acceptable for LSCI because de-correlation of the speckle pattern was consistently present under flow conditions. Thus, the comparable results observed between the traditional LSCI components and the inexpensive counterparts indicate that the latter may be used with relative accuracy as long as minimum image quality is achieved.

One of the major advantages of the low-cost LSCI components is the compact size and weight of the overall setup. The total length of the LSCI instrumentation from the top of the camera to the edge of the lens system was 5.6 cm. Customizing the mounting components used for holding the lenses could reduce this length further, since we had to choose the minimum focal length of the lenses based on the dimensions of the mounting components. Having a compact setup can be useful for many reasons, including ease of integration with other techniques and portability. The weight of the LSCI instrumentation was 25 g, and this could be improved with further customization as well. A lightweight setup could make LSCI an even easier add-on feature for systems where weight is a concern, such as integration with surgical microscopes and robotic systems used in clinical medicine. A low-cost, compact setup that is easily portable could also increase access to the technology for global health care applications.

5. Conclusions

This paper demonstrates that very inexpensive instrumentation (\$90) can be used to image microcirculatory flows with accuracy comparable to a traditional LSCI system. The accuracy of the webcam was validated using a high performance monochrome CCD camera, and excellent agreement was exhibited both *in vitro* and *in vivo*. Overall, this study illustrates that comparable blood flow images can be acquired using a low-cost LSCI system, indicating that expensive components may not necessarily be required. By reducing the costs, LSCI will be more accessible to both scientific researchers and clinicians, thus enabling more widespread adoption of this valuable technique.

Acknowledgments

The authors would like to acknowledge Yu-Yen Huang and Ehssan Faraji for their help fabricating the microfluidic phantom used in this study. This work was funded by grants from The Coulter Foundation, The National Institutes of Health (EB011556, NS078791), and The National Science Foundation (CBET/0737731).